Joint probabilities and mixing of isolated scalars emitted from parallel jets

M. A. Soltys[1] and J. P. Crimaldi[1],†

[1]Department of Civil, Environmental and Architectural Engineering,
University of Colorado, Boulder, CO 80309-0428, USA

Mixing and reaction between two scalars initially separated by scalar-free ambient fluid is important in problems ranging from ecology to engineering. Using a two-channel planar laser-induced fluorescence (PLIF) system the instantaneous spatial structure of two independent scalars emitted from parallel jets into a slow coflow is quantified. Of particular interest is the scalar covariance used to define the correlation coefficient. Joint probability distribution functions (JPDFs) and instantaneous images of the scalar fields demonstrate that initially the flow mainly consists of incursions of fluid from one jet into the other, and *vice versa*, before scalars have time to assemble in attracting regions of the flow and coalesce due to diffusive flux. Decomposing the joint probability distribution exhibits the effect these events have on scaler overlap and scalar covariance. Along the centreline near where the mean profiles of the jets meet, the scalar covariance is negative; however, the covariance becomes positive as the scalars converge in shared structure and diffusive flux bridges a reduced barrier of ambient fluid. The mixing path between scalar filaments can be probabilistically observed through the conditional diffusion of the two scalars at various points in the flow.

Key words: jets, reacting flows, turbulent mixing

1. Introduction

1.1. *Reactive and non-reactive mixing*

The overwhelming majority of studies of two-scalar mixing and reaction consider only the condition where the two scalars initially share a material interface. In this binary topology, fluid stirring necessarily stretches the shared interface, sharpens scalar gradients and increases diffusive flux normal to the interface, and thus enhances mixing and any reaction between the two scalars. However, if the two scalars are initially separated by ambient fluid, the role of stirring on subsequent mixing and/or reaction is more complex. For efficient mixing or reaction to occur in the latter scenario, the flow must first locally aggregate filaments of the two scalars such that diffusion can bridge a substantially reduced barrier of ambient fluid. The processes that permit this aggregation are not well understood, despite the fundamental nature of this problem. In this study, we examine mixing and reaction (in the low-Damköhler

† Email address for correspondence: Crimaldi@colorado.edu

limit) between two parallel turbulent jets, each marked with a different scalar and separated by a finite transverse distance. We examine the role of instantaneous stirring processes on resulting probabilities of local co-occurring concentrations to develop a framework for understanding how stirring influences mixing and reaction between the two initially distant scalars.

Using simple second-order reaction kinetics, the dimensional reaction product is (Mao & Toor 1971)

$$\widetilde{\Theta} = k\widetilde{\Phi_A}\widetilde{\Phi_B}, \tag{1.1}$$

where k is a reaction rate constant and $\widetilde{\Phi_A}$ and $\widetilde{\Phi_B}$ are the local concentrations of the reactants. Although higher-order reactions have more complicated reaction kinetics, the physics of how two reactive scalars coalesce are essentially the same (Komori *et al.* 1991). In the low-Damköhler limit (i.e. when the reaction is very slow), the reaction has a negligible effect on the existing scalar fields, and conserved scalars are meaningful proxies for studying the dynamics of stirring for reactive scalars (Crimaldi, Cadwell & Weiss 2008). Thus, in the present paper the local non-dimensional scalar overlap $\Phi_A\Phi_B$ will be used to quantify mixing between the two scalars. This scalar overlap quantifies the role of fluid stirring on the local reaction production in (1.1).

When scalar concentrations are decomposed into mean and fluctuating terms ($\Phi = \langle\Phi\rangle + \phi'$), the time-averaged scalar overlap can be written as (e.g. Cetegen & Sirignano 1990; Crimaldi, Hartford & Weiss 2006)

$$\langle\Phi_A\Phi_B\rangle = \langle\Phi_A\rangle\langle\Phi_B\rangle + \langle\phi'_A\phi'_B\rangle, \tag{1.2}$$

where the first term on the right-hand side is the product of the mean concentrations and the second term is the scalar covariance. The scalar covariance defines correlation between the fields of Φ_A and Φ_B and quantifies the average contributions of instantaneous processes to the scalar overlap. In both reactive and non-reactive cases, the instantaneous contributions from the scalar covariance are essential to define mixing or reaction between the two scalars. A comprehensive understanding of how the scalar covariance forms and evolves is essential in understanding turbulent mixing processes between multiple scalars.

The scalar covariance is commonly normalized as the correlation coefficient (e.g. Sirivat & Warhaft 1981)

$$\rho = \frac{\langle\phi'_A\phi'_B\rangle}{\left(\langle\phi'^2_A\rangle\langle\phi'^2_B\rangle\right)^{1/2}}, \tag{1.3}$$

where $\langle\phi'^2_A\rangle$ and $\langle\phi'^2_B\rangle$ are the scalar variances. The correlation coefficient is bounded by $-1 \leqslant \rho \leqslant 1$, where $\rho = -1$ and $\rho = 1$ indicate perfect linear anticorrelation and correlation, respectively.

1.2. *Binary and isolated topology*

In the binary topology (where two scalars initially share a material interface) the mass fractions of the two conservative scalars must sum to unity, $\Phi_A + \Phi_B = 1$, and scalar covariance can be defined in terms of the variance of a single scalar,

$$\langle\phi'_A\phi'_B\rangle = -\langle\phi'^2_A\rangle = -\langle\phi'^2_B\rangle. \tag{1.4}$$

This implies that $\rho = -1$ everywhere in the flow and knowledge of the concentration of a single scalar can be used to infer the concentration of the other.

In contrast to the binary topology, many flow scenarios exist where the two scalars of interest are separated by a third ambient fluid (Crimaldi & Browning 2004; Crimaldi *et al.* 2006, 2008; Crimaldi 2012; Crimaldi & Kawakami 2013). The scalar covariance in this topology can be indirectly computed using measurements of each individual scalar, followed by measurements of the combined scalar field (Warhaft 1984)

$$2\left\langle \phi'_A \phi'_B \right\rangle = \left\langle \left(\phi'_A + \phi'_B \right)^2 \right\rangle - \langle \phi'^{\,2}_A \rangle - \langle \phi'^{\,2}_B \rangle. \tag{1.5}$$

The method of inference has been used to calculate covariance between multiple scalar mixing in a variety of flows including grid turbulence (Stapountzis 1988), boundary layer flows (Sawford, Frost & Allan 1985; Davies & Jones 2000), jet flows (Tong & Warhaft 1995), and turbulent channel flow (Costa-Patry & Mydlarski 2008). Although this method permits quantification of the scalar covariance in a number of flows, it lends no insight into the direct role of instantaneous flow processes on the development of scalar covariance. In the present study we overcome this limitation by directly measuring instantaneous fields of $\phi'_A \phi'_B$ and can observe how instantaneous structures affect the covariance.

1.3. *Probability distributions*

The probability distribution function (PDF) for each scalar $P(\Phi)$ and more specifically the joint probability distribution function (JPDF) between two scalars $P(\Phi_A, \Phi_B)$ contain all of the statistical moments for each scalar and scalar interactions at a point in a flow. Because of the wealth of information contained in the PDFs, they have been widely used to estimate unclosed terms, including scalar covariance, in turbulence models (e.g. Pope 1985; Mitarai, Riley & Kosály 2005).

The form of the single-scalar PDF $P(\Phi)$ varies widely in the literature and depends on many factors including boundary conditions, flow geometry, nature of turbulence, the Schmidt number of the scalars, etc. Studies involving the transport of heat in jets (Venkataramani, Tutu & Chevray 1975) revealed Gaussian-shaped scalar PDFs; however, many studies since have suggested non-Gaussian shapes. Eswaran & Pope (1988) computed numerical simulations of one scalar in two states ($\Phi = -1$ or $\Phi = 1$) and found the scalar PDF to have a bimodal distribution that relaxed to a Gaussian distribution between the two initial states at longer timescales. In the near field, scalar PDFs have also been described using beta distributions (Girimaji 1991; Beta *et al.* 2003), gamma distributions (Villermaux & Duplat 2003; Villermaux 2004), Gaussians with exponential tails (Jayesh & Warhaft 1991) and skewed Gaussians (Dahm & Dimotakis 1990).

Similar to $P(\Phi)$, the two-scalar JPDF $P(\Phi_A, \Phi_B)$ varies greatly according the flow geometry, nature of turbulence, separation distance between scalars and scalar Schmidt number. JPDFs are reported for homogenous isotropic turbulence (Juneja & Pope 1996), scalar mixing layers (Bilger, Saetran & Krishnamoorthy 1991; Sawford & de Bruyn Kops 2008) and coaxial jets (Cai *et al.* 2011; Rowinski & Pope 2013). In the binary scalar topology, the mixing path between the two scalars falls on a straight line where $\Phi_A + \Phi_B = 1$ (Sawford & de Bruyn Kops 2008). In the isolated topology, scalars must first mix with ambient fluid before mixing with each other (Cai *et al.* 2011). The result is the mixing path between the two scalars must first make a detour toward the ambient state (Sawford & de Bruyn Kops 2008; Cai *et al.* 2011); however, the size and shape of this detour depends on the separation between the scalars and the nature of the turbulence. For reactive flows, the mixing path also

depends on travel time and reactivity of the two scalars expressed as the Damköhler number (Bilger *et al.* 1991). As the scalars become well-mixed at long timescales, $P(\Phi_A, \Phi_B)$ approaches a joint-normal distribution (Juneja & Pope 1996).

The evolution of the JPDF in homogeneous flows is defined in terms of the conditional diffusion (Juneja & Pope 1996),

$$\frac{\partial P(\Phi_A, \Phi_B)}{\partial t} = -\frac{\partial}{\partial \Phi_i} \left[P(\Phi_A, \Phi_B) \, \gamma_i(\Phi_A, \Phi_B) \right], \tag{1.6}$$

where the conditional diffusion $\gamma_i(\Phi_A, \Phi_B)$ is defined as the conditional expectation

$$\gamma_i(\Phi_A, \Phi_B) = \left\langle D_i \nabla^2 \Phi_i \,|\, (\Phi_A, \Phi_B) \right\rangle. \tag{1.7}$$

In scalar space the conditional diffusion has two vector components, γ_A and γ_B, describing the transport velocity of the JPDF (Cai *et al.* 2011). The magnitude and direction of the conditional diffusion is important as it describes not only the mixing path of the two scalars, but also the speeds of various mixing processes in the flow.

1.4. *Turbulent jets*

Turbulent jets are a prototypical flow for studying turbulence structure (e.g. Crow & Champagne 1971; Hussein, Capp & George 1994; Ball, Fellouah & Pollard 2012) and scalar mixing (e.g. Tong & Warhaft 1995; Catrakis & Dimotakis 1996; Warhaft 2000). Interactions between multiple jets are a natural extension of this fundamental problem and are of interest for mixing studies in the areas of combustion, chemical mixing, pollutant transport and environmental processes. Velocity fields for multiple jets have been studied for inclined jets (Becker & Booth 1975; Wang, Lin & Sheu 1993; Villafruela, Castro & Parra 2008), coaxial jets (Champagne & Wygnanski 1971) and parallel jets both experimentally (Yuu, Shimoda & Jotaki 1979; Pani & Dash 1983; Lin & Sheu 1990; Anderson & Spall 2001; Fujisawa, Nakamura & Srinivas 2004; Bunderson & Smith 2005) and numerically (Spall, Anderson & Allen 2004; Zarruk & Cowen 2008).

For parallel jets, also referred to as 'twin jets' and 'dual jets' (Erdem & Atl 2002), three regions are commonly defined. Beginning at the origin, the converging region is defined where the velocity fields of both jets are separate and a recirculating flow is found between the two. The merging region extends from the point where the streamline velocity is zero until it reaches its maximum. In this region, transverse profiles of the streamwise velocity have two peaks that move closer together. At the point after the velocity in the streamwise direction is maximum, the mean velocity field of the two jets resembles that of a single jet (i.e. Gaussian), and measurements of mean and fluctuating velocity profiles are self-similar (Erdem & Atl 2002).

Scalar fields have been measured in multiple plane jets (Grandmaison & Zettler 1989) and multiple round jets (Hodgson, Moawad & Rajaratnam 1999; Wang & Davidson 2003). Stapountzis *et al.* (1992) studied the reaction product of two scalars emitted from parallel jets, but did not quantify the reactant fields themselves. The study suggests if jet velocities, scalar diffusivities and reactivities are symmetric, the reactant field will be Gaussian in profile. Fujisawa *et al.* (2004) visualized mixing between two parallel jets with different velocities, but did not calculate reaction or correlation statistics. Duplat & Villermaux (2008) visualized two scalars from parallel jets in a small duct. PDFs of the individual scalars were skewed Gaussian, and were used to create the inference PDF of the combined scalar field.
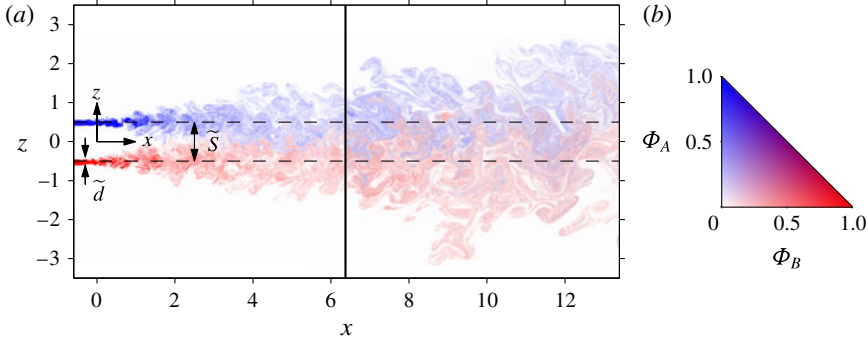
FIGURE 1. (*a*) Instantaneous image from $Re = 1500$ and $\widetilde{S} = 2.5$. The vertical line indicates the division between upstream and downstream images, while the horizontal dashed lines indicate the location of the centerline of each jet. The jet diameter $\widetilde{d}$, spacing $\widetilde{S}$, as well as the virtual origin are denoted. The colour map used to display the data is shown (*b*) where the concentrations are normalized by the initial jet fluid concentration.

	Low $Re = 750$	High $Re = 1500$
Close $\widetilde{S} = 1.4$ cm		$\widetilde{u} = 40$ cm s^{-1} $\widetilde{Q} = 280$ ml min^{-1}
Far $\widetilde{S} = 2.5$ cm	$\widetilde{u} = 20$ cm s^{-1} $\widetilde{Q} = 138$ ml min^{-1}	$\widetilde{u} = 40$ cm s^{-1} $\widetilde{Q} = 280$ ml min^{-1}

TABLE 1. Experimental conditions for the three cases in the present study.

The present study uses a two-channel planar laser-induced fluorescence (PLIF) technique to measure two initially isolated conserved scalars emitted by parallel round jets. The scalars can be simultaneously and independently measured to give mixing statistics, including ρ, as well as higher-order statistics in the form of the JPDF $P(\Phi_A, \Phi_B)$ and the conditional diffusion γ_i. These statistics are examined in parallel with instantaneous images to understand the physics of how the two scalars come together, and how instantaneous processes cause scalar covariance to evolve.

2. Experimental approach

Two parallel round jets with separation $\widetilde{S}$, each marked with a separate scalar, issue into the ambient fluid of a recirculating flume (figure 1). Jet spacing and Reynolds number were varied in the present study as shown in table 1. The jets consist of 2.75 m of straight 0.39 cm diameter round tubing oriented horizontally into the ambient flow. The viscosity of the fluid was 1.04×10^{-6} m^2 s^{-1}. The test section of the recirculating flume is 0.4 m deep $\times$ 1.25 m wide.

The flow of the jet fluid was driven using two matching pulseless gear pumps. The long development length of the jet tubing ($>700\widetilde{d}$) provides a fully developed velocity profile (Durst *et al.* 2005). A slow laminar and shear-free ambient coflow of 0.37 cm s^{-1} was passed through the test section to prevent accumulation of jet fluid. The ambient flow first passed through a 15 cm thick honeycomb with 0.69 cm diameter cells just upstream of the jet exits. The coflow velocity was less than 2 % of the mean jet velocity at the low Reynolds number, and thus its affect on the turbulent jet structure is assumed to be minimal in the test section (Nickels & Perry 1996).

The jets exit with a parabolic velocity profile and transition to turbulent jets a short distance downstream. For purposes of self-similarity we define a location to be used as a virtual origin for subsequent analysis. This point is defined by performing a linear fit to the inverse centreline concentration of the two jets and the resulting x-intercept defines $\widetilde{x} = 0$ (Zarruk & Cowen 2008). The centreline between the two jets is denoted as $\widetilde{z} = 0$. In figure 1, and throughout the rest of this paper, axes are non-dimensionalized by the jet spacing as $x = \widetilde{x}/\widetilde{S}$ and $z = \widetilde{z}/\widetilde{S}$.

The jets were imaged using a two-channel PLIF system that simultaneously and independently measures the two scalar fields. Details of the technique, including the acquisition and processing of image data are outlined in Soltys & Crimaldi (2011). Beams from separate lasers (argon-ion and krypton-ion) are combined to form a single light sheet 0.5 mm wide that passes vertically through the axis of each jet. The top jet was marked with fluorescein ($\widetilde{\Phi}_0 = 0.05$ p.p.m.), which is excited by the 488 nm line of the argon-ion laser. The bottom jet was marked with oxazine ($\widetilde{\Phi}_0 = 0.25$ p.p.m.), which is excited by the 647 nm line of the krypton-ion laser. Both concentrations were sufficiently low to be optically thin (Melton & Lipp 2003) and were normalized by the concentration at the jet exit as $\Phi = \widetilde{\Phi}/\widetilde{\Phi}_0$. Tests showed that the laser sheet was sufficiently thin to produce converged scalar statistics (Soltys & Crimaldi 2011). Two cameras with optical filters matched to the emission spectra of each dye recorded instantaneous fluorescence from the two dyes with a pixel resolution of 0.14 cm pixel^{-1}.

Data was collected for two adjacent 20.0 cm × 14.8 cm regions with 4.8 cm of overlap between the upstream and downstream regions. In figure 1 the vertical line denotes the separation between the upstream and downstream dataset; however, in subsequent figures no distinction between the two datasets for each flow case will be made. One thousand image pairs were captured at a frame rate of 2 Hz for each Reynolds number (defined based on the exit velocity and nozzle diameter), jet spacing and streamwise location.

Images from each camera were then post-processed to rectify the images to the same plane and correct for errors caused by fluorescence from background dye, fluorescence saturation, laser attenuation, spatial variation in the light sheet, lens vignette and variations in gain and offset using a robust image processing algorithm outlined in Soltys & Crimaldi (2011). The algorithm

$$\Phi_{A,n} = b_{A,n} \frac{I_{A,n} - B_{A,n}}{B_{A,n} - D_A} \tag{2.1}$$

corrects the intensity field for the nth image, I_n, using the background dye concentration for the nth image, B_n, interpolated from images before and after the experiment and the camera dark response, D. If one-directional cross-talk from channel A (i.e. fluorescein) to channel B (i.e. oxazine) occurs, equation (2.1) can be corrected as

$$\Phi_{B,n} = b_{B,n} \frac{I_{B,n} - B_{B,n} - \lambda \left[I_{A,n} - B_{A,n} \right]}{B_{B,n} - D_B - \lambda \left[B_{A,n} - D_A \right]} \tag{2.2}$$

where λ is the cross-talk occurring from channel A to channel B. Because stokes fluorescence only occurs from shorter wavelengths to longer wavelengths, cross-talk will only occur in one direction. The constant λ varies based on parameters of the system such as camera spectral sensitivity, relative laser power for both lasers and the pH of the fluid. Therefore, λ is determined from a separate experiment with a
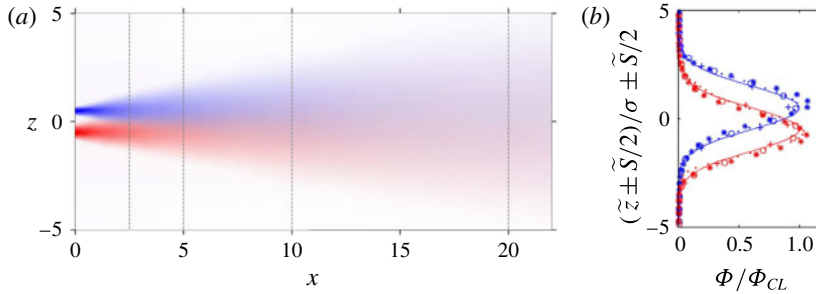
FIGURE 2. (*a*) Spatial distribution of $\langle \Phi_A \rangle$ and $\langle \Phi_B \rangle$ for $Re = 1500$ and $\widetilde{S} = 1.4$ cm. The colour map is the same as in figure 1(*b*). (*b*) Normalized transverse profiles at $x = 2.5$ (+), 5 (○), 10 (*) and 20 (·) indicated by grey dashed lines in the left. Solid lines are Gaussian profiles centred at each jet axis.

single fluorescein jet, while b_1 and b_2 were calibrated using images of known uniform concentrations of fluorescein and oxazine.

The images are recombined into a single image (e.g. figure 1) with the colour map shown in figure 1(*b*). The colour map uniquely displays concentrations of the individual scalars, as well as any combination of the two. The concentration of the upper jet, Φ_A, is shown in varying tints of blue while the lower jet, Φ_B, is shown in varying tints of red. Ambient fluid is shown as white, and any mixture of Φ_A and Φ_B is displayed as a unique hue of purple. All possible mixtures are contained in the triangular region of figure 1(*b*).

3. Results

Typical spatial distributions of the scalar means $\langle \Phi_A \rangle$ and $\langle \Phi_B \rangle$ are shown in figure 2(*a*) for high Reynolds number and close jet spacing. Figure 2(*b*) shows normalized transverse profiles for both Reynolds numbers at the far jet spacing at locations denoted by grey dashed lines in figure 2(*a*). The profiles are normalized by plume width σ and centreline concentration Φ_{CL} based on Gaussian fits to the data. The mean plumes are Gaussians centred at $x = 0.5$ and $x = -0.5$ for Φ_A and Φ_B, respectively. The solid lines in figure 2(*b*) are Gaussian profiles centred at each jet axis. The close fit of the data to the Gaussian profiles suggests the mean jet flows see little influence from interactions with the opposite jet.

In (1.2), we show that the time-averaged scalar overlap $\langle \Phi_A \Phi_B \rangle$ can be decomposed into the sum of the product of the mean concentrations $\langle \Phi_A \rangle \langle \Phi_B \rangle$ and the scalar covariance $\langle \phi'_A \phi'_B \rangle$. Figure 3 shows the streamwise development of transverse profiles of each of these three terms. Due to the fact that both $\langle \Phi_A \rangle$ and $\langle \Phi_B \rangle$ are Gaussian and equally spaced about $z = 0$, the product of the two, $\langle \Phi_A \rangle \langle \Phi_B \rangle$, will also be a Gaussian centred at $z = 0$. Here $\langle \Phi_A \Phi_B \rangle$ also has a Gaussian appearance and thus the scalar covariance term can be approximated as the difference of two Gaussians. In figure 3, solid lines are Gaussian fits to $\langle \Phi_A \Phi_B \rangle$ and $\langle \Phi_A \rangle \langle \Phi_B \rangle$, and to the difference of the two Gaussians for $\langle \phi'_A \phi'_B \rangle$.

At $x = 2.5$, a positive Gaussian of the product $\langle \Phi_A \rangle \langle \Phi_B \rangle$ forms as Φ_A and Φ_B begin to reach the centerline between the two jets. Here $\langle \Phi_A \Phi_B \rangle$ is also Gaussian with an amplitude approximately half that of $\langle \Phi_A \rangle \langle \Phi_B \rangle$ and a slightly larger width. Because $\langle \Phi_A \Phi_B \rangle$ and $\langle \Phi_A \rangle \langle \Phi_B \rangle$ vary in width and magnitude, the scalar covariance has both
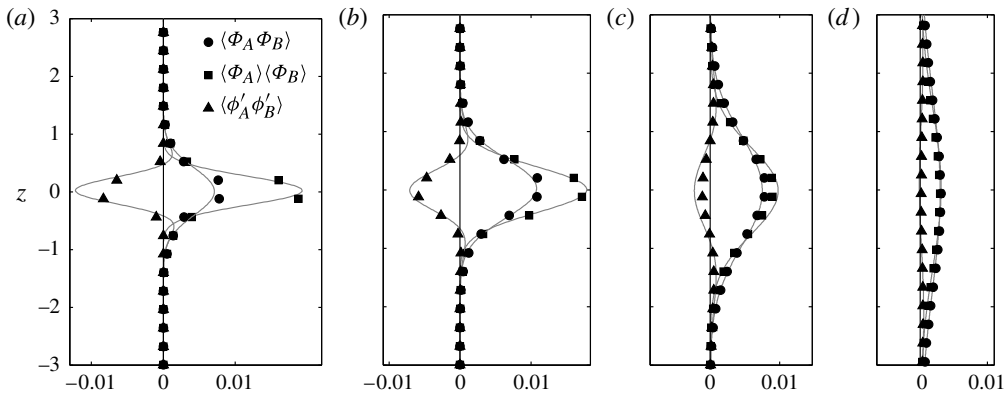
FIGURE 3. Profiles of the time-averaged scalar overlap $\langle \Phi_A \Phi_B \rangle$, the product of the scalar means $\langle \Phi_A \rangle \langle \Phi_B \rangle$, and the scalar covariance $\langle \phi_A' \phi_B' \rangle$ at (*a*) $x = 2.5$, (*b*) $x = 5$, (*c*) $x = 10$ and (*d*) $x = 20$ for $Re = 1500$ and $\widetilde{S} = 1.4$ cm. The grey lines are Gaussians fitted to the data, or to the difference of two Gaussians in the case of the scalar covariance.

positive and negative regions. The majority of the scalar covariance at this point is negative, with a local minimum at $z = 0$. Small positive regions exist near $z = \pm 0.7$.

Farther downstream at $x = 5$, coalescence between the two scalars has continued to increase. $\langle \Phi_A \rangle \langle \Phi_B \rangle$ has widened and decreased in magnitude as the scalars mix across y and z. The scalar covariance increases in magnitude everywhere with positive regions centred near $z = \pm 1$. At $x = 10$ both $\langle \Phi_A \rangle \langle \Phi_B \rangle$ and $\langle \Phi_A \Phi_B \rangle$ have decreased and more notable positive regions are visible in $\langle \phi_A' \phi_B' \rangle$. By $x = 20$, the peak of $\langle \Phi_A \rangle \langle \Phi_B \rangle$ is smaller than that of $\langle \Phi_A \Phi_B \rangle$, and $\langle \phi_A' \phi_B' \rangle$ is positive, albeit small, everywhere.

Figure 4 displays the streamwise evolution of $\langle \Phi_A \Phi_B \rangle$, $\langle \Phi_A \rangle \langle \Phi_B \rangle$, and $\langle \phi_A' \phi_B' \rangle$ along the centreline between the two jets for both Reynolds numbers and spacings. The scalar overlap reaches a maximum near $x \approx 4$ for the close spacings and near $x \approx 6$ for the far spacings. Here $\langle \Phi_A \Phi_B \rangle$ is higher for close nozzle spacing and high Reynolds numbers and $\langle \Phi_A \rangle \langle \Phi_B \rangle$ is greater than $\langle \Phi_A \Phi_B \rangle$ until $x \approx 17$ with local maximums occurring slightly upstream of the peak reaction. The scalar covariance in this region is negative with local minimums near $x = 3$ for the close spacing and $x = 4$ for the far spacing. Downstream of $x \approx 17$, the product of the mean scalar concentrations is lower than the mean reaction and $\langle \phi_A' \phi_B' \rangle$ becomes positive.

The spatial distribution of the correlation coefficient ρ is shown in figure 5. The correlation coefficient highlights the spatial evolution of the scalar covariance by normalizing it by the variance of each scalar (1.3). Near the source the centreline region is dominated by negative correlations, with positive correlations occurring off the centreline (compare with figures 3 and 4). Progressing downstream, ρ increases in magnitude, becoming positive at the centreline near $x \approx 17$. Far from the centreline and far downstream, ρ tends to unity as the scalar covariance and the product of the variances vanish at equal rates (Tong & Warhaft 1995; Viswanathan & Pope 2008). Mixing still occurs between the two jets along the centreline (figure 4) even though negative correlations dominate in these regions.

3.1. *Instantaneous fields*

Representative instantaneous scalar fields are shown for upstream (figure 6*a*) and downstream (figure 7*a*) locations. The spatial scale varies between the two figures,
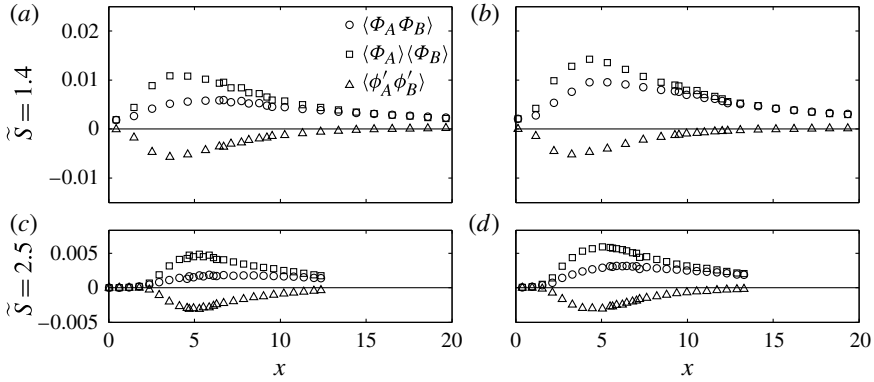
FIGURE 4. Streamwise evolution along the centreline ($z=0$) of the scalar overlap $\langle \Phi_A \Phi_B \rangle$, the product of the means $\langle \Phi_A \rangle \langle \Phi_B \rangle$ and the scalar covariance $\langle \phi'_A \phi'_B \rangle$ shown for both spacings (rows) and Reynolds numbers (columns): (a,c) $Re = 750$; (b,d) $Re = 1500$.
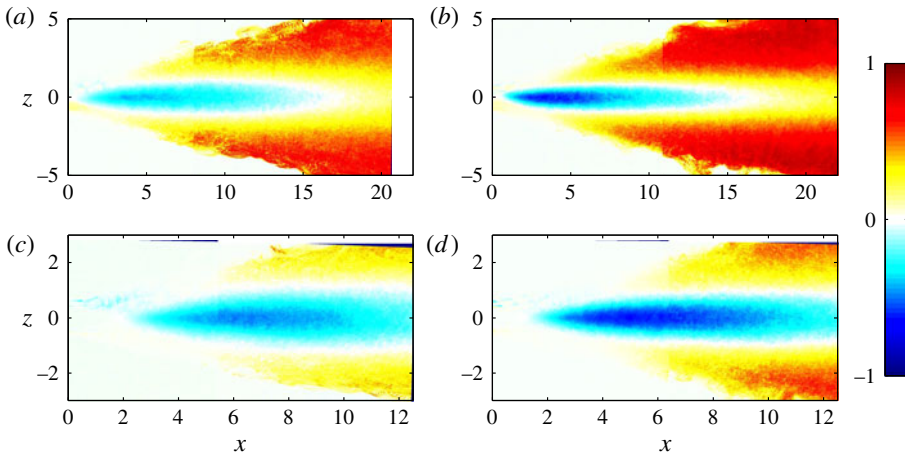

FIGURE 5. Time averaged correlation coefficient ρ. Here $Re = 750$ is displayed in the (a,c) and $Re = 1500$ is displayed on (b,d), while the $\widetilde{S} = 1.4$ cm in (a,b) and $\widetilde{S} = 2.5$ cm in (c,d).

but both share the same colour map as figure 1(b). As the jets spread toward one another in the upstream region, coherent flow structures from one jet transport the scalar from that jet transversely into the second jet, displacing the second scalar. These scalar incursions are initially insulated from contact with the second scalar by a buffer of ambient fluid (e.g. figure 6a $x = 1.8$, $z = 0.2$). As the incursions advect downstream they are stirred by local structures in the resident jet, thinning the buffer of ambient fluid and enabling diffusion to promote overlap between the two scalars. Farther downstream (figure 7a) the velocity and scalar fields of the two jets have largely merged across the domain, although the scalars remain somewhat segregated at small scales due to combined effects of the ambient fluid buffer and the weak scalar diffusivities.

The resulting instantaneous scalar overlap as quantified by $\Phi_A \Phi_B$ is shown in figures 6(b) and 7(b). Note that both the spatial scales and color maps differ between
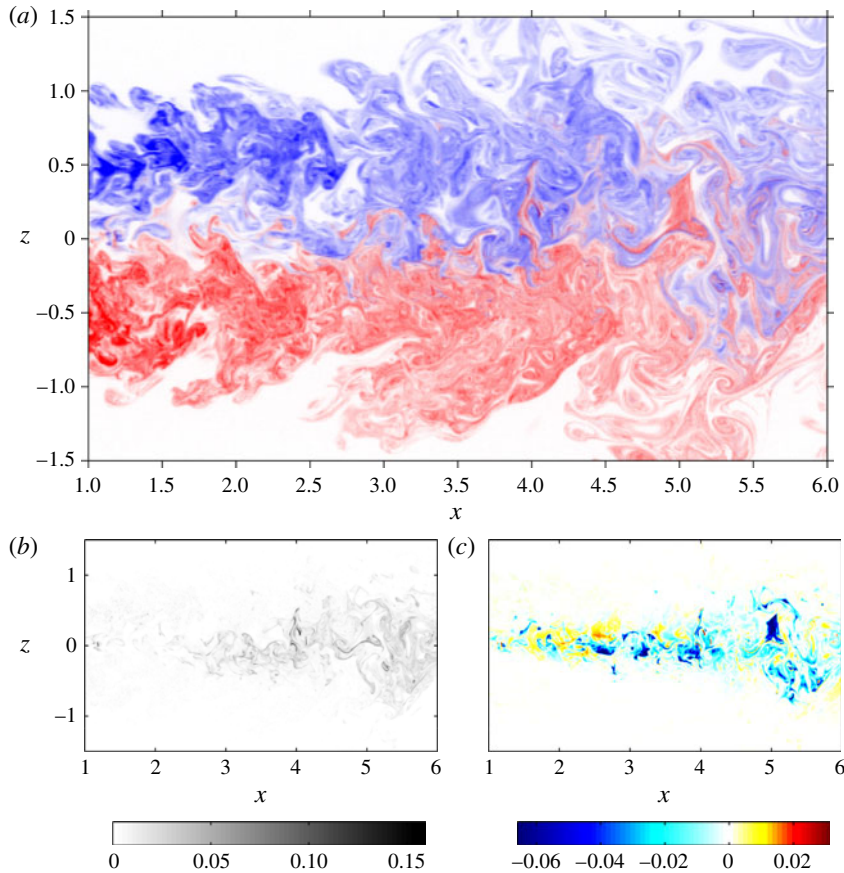
FIGURE 6. (*a*) Instantaneous concentrations Φ_A and Φ_B for $Re = 1500$ and $\widetilde{S} = 1.4$ using the same colour map as figure 1. (*b*) Instantaneous contributions to the scalar overlap $\Phi_A\Phi_B$. (*c*) Instantaneous contributions to the scalar covariance $\phi'_A\phi'_B$.

the two figures. The overlap is close to zero far upstream, but grows downstream and spreads transversely. Strong local occurrences of $\Phi_A\Phi_B$ are seen to be associated with with scalar incursions shown in figure 6(*a*) (e.g. $x = 4$, $z = 0.25$) that continue to be stirred and mixed as shown in figure 7(*a*) (e.g. $x = 14.5$, $z = 2.75$).

The instantaneous contributions to the scalar covariance $\phi'_A\phi'_B$ are shown in figures 6(*c*) and 7(*c*). Again both the spatial scales and colour maps differ between the two figures. Incursions of one scalar displacing the other are responsible for strong negative contributions to the scalar covariance (e.g. figure 6*c*). Positive contributions occur in regions where both scalars overlap in concentrations above the local mean concentrations (e.g. figure 7*c* $x = 14.5$, $z = 2.75$), or where ambient fluid dominates.

Figures 6 and 7 give insight into the spatial evolution of ρ (figure 5), suggesting displacement events resulting in negative correlations are common near the centreline for $x < 17$. Farther downstream and off the centreline, incursions continue to be stirred and mixed and positive correlations are more likely. Although the images provided only contain a few representative cases of structures contributing to the scalar covariance, the detailed discussion of the probabilities of these events in the following section can give more insight into the flow-field.
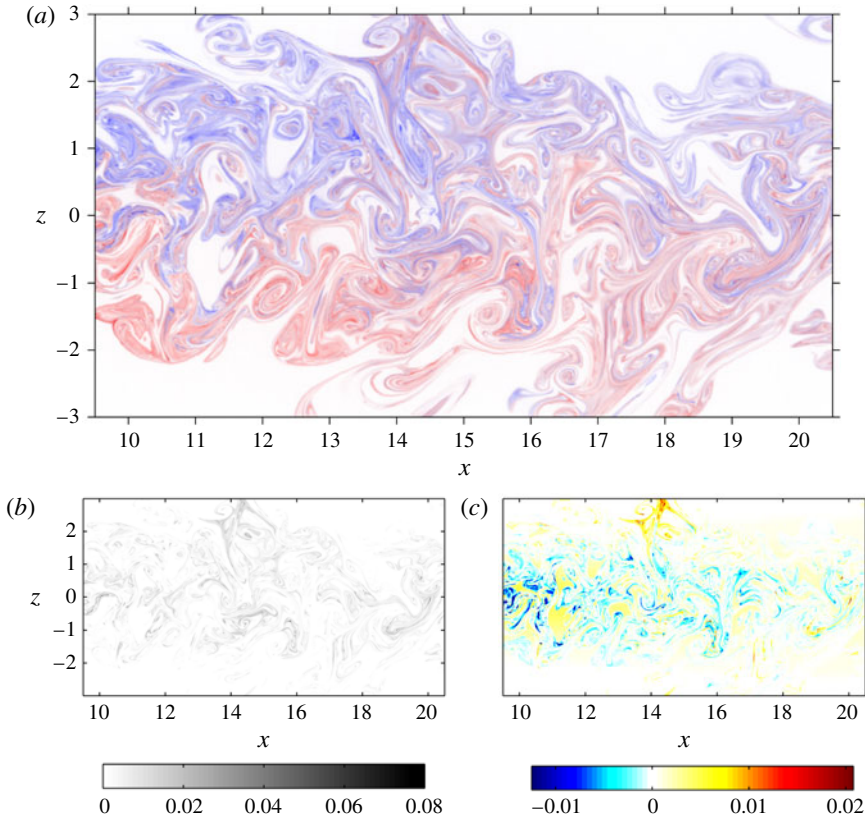
FIGURE 7. (*a*) Instantaneous concentrations Φ_A and Φ_B for $Re = 750$ and $\widetilde{S} = 1.4$ using the same colour map as figure 1. (*b*) Instantaneous contributions to the scalar overlap $\Phi_A \Phi_B$. (*c*) Instantaneous contributions to the scalar covariance $\phi'_A \phi'_B$.

3.2. *Joint probability distribution functions*

The JPDF $P(\Phi_A, \Phi_B)$ (e.g. figures 8–10) quantifies the probability of various mixtures of Φ_A, Φ_B, and ambient fluid at a given location in the flow. Upstream of the virtual origin ($x \leqslant 0$), the scalar space consists of three distinct states: $(\Phi_A, \Phi_B) = (1, 0)$ inside the scalar A jet, $(\Phi_A, \Phi_B) = (0, 1)$ inside the scalar B jet, or $(\Phi_A, \Phi_B) = (0, 0)$ in pure ambient fluid. As Φ_A and Φ_B each initially mix with surrounding ambient fluid, contributions to $P(\Phi_A, \Phi_B)$ evolve along the Φ_A and Φ_B axes toward the origin. The interior of the scalar space becomes populated only as Φ_A and Φ_B diffuse across the ambient buffer and mix with each other. Since both jets must first mix with ambient fluid, it is not possible for $P(\Phi_A, \Phi_B)$ to evolve directly along the line $\Phi_A + \Phi_B = 1$ that connects $(0, 1)$ and $(1, 0)$.

We present $P(\Phi_A, \Phi_B)$ for a number of specific locations in each flow. For smoothing purposes each location represents statistics averaged over a 2 mm × 2 mm region. We take advantage of geometric symmetry and present $P(\Phi_A, \Phi_B)$ only for $z \geqslant 0$. Data from $z < 0$ is averaged with the $z > 0$ data after being mirrored in scalar space across the line $\Phi_A = \Phi_B$.

In figures 8–12, contours containing 80 %, 60 %, 40 % and 20 % of the total probability are shown for each plot, and are shaded with the darker regions indicating
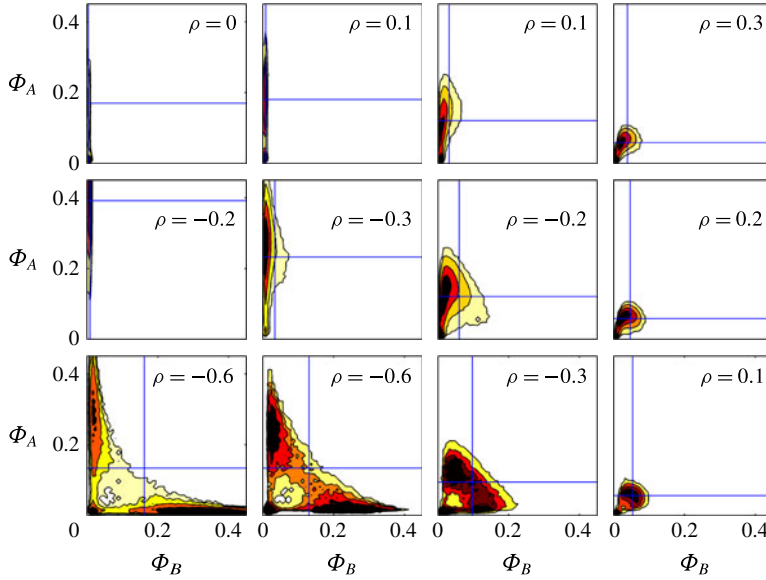
FIGURE 8. The JPDF $P(\Phi_A, \Phi_B)$ for $Re = 1500$ and $\widetilde{S} = 1.4$ cm displayed at $z = 0$, 0.5 and 1 (rows) and $x = 2.5$, 5, 10 and 20 (columns). Probabilities are shown on a log scale with contours containing 80 %, 60 %, 40 %, and 20 % of the data. Blue lines show the mean concentrations $\langle \Phi_A \rangle$ and $\langle \Phi_B \rangle$.
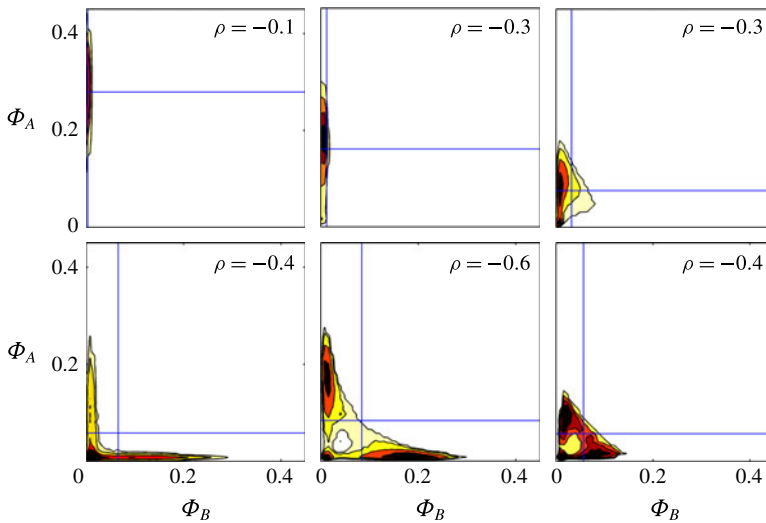

FIGURE 9. The JPDF $P(\Phi_A, \Phi_B)$ for $Re = 1500$ and $\widetilde{S} = 2.5$ cm displayed at $z = 0$ and 0.5 (rows) and $x = 2.5$, 5 and 10 (columns). Probabilities are shown on a log scale with contours containing 80 %, 60 %, 40 % and 20 % of the data. Blue lines show the mean concentrations $\langle \Phi_A \rangle$ and $\langle \Phi_B \rangle$.

events of higher probability. The local means $\langle \Phi_A \rangle$ and $\langle \Phi_B \rangle$ are indicated by horizontal and vertical blue lines, and the local correlation coefficient is listed in the upper corner of each plot.
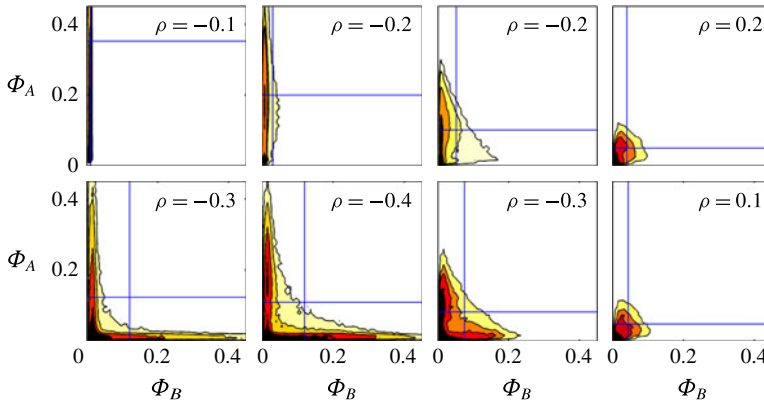
FIGURE 10. The JPDF $P(\Phi_A, \Phi_B)$ for $Re = 750$ and $\widetilde{S} = 1.4$ cm displayed at $z = 0$ and 0.5 (rows) and $x = 2.5$, 5, 10 and 20 (columns). Probabilities are shown on a log scale with contours containing 80 %, 60 %, 40 % and 20 % of the data. Blue lines show the mean concentrations $\langle \Phi_A \rangle$ and $\langle \Phi_B \rangle$.
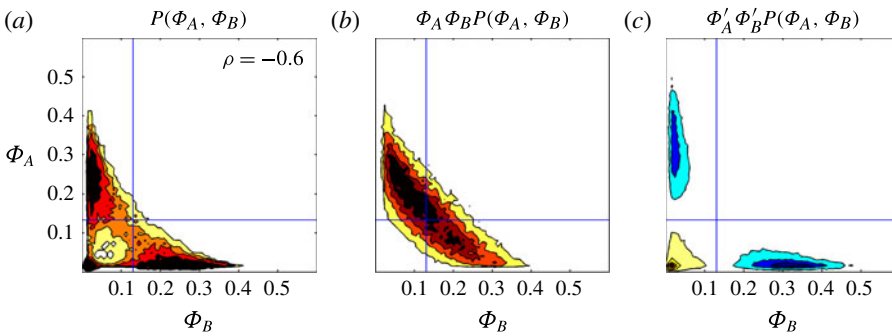

FIGURE 11. (*a*) The JPDF $P(\Phi_A, \Phi_B)$ for $Re = 1500$ and $\widetilde{S} = 1.4$ cm at $x = 5$, $z = 0$. Probabilities are shown on a log scale with contours containing 80 %, 60 %, 40 % and 20 % of the data. (*b*) Corresponding contributions to $\langle \Phi_A \Phi_B \rangle$ contoured to show 80 %, 60 %, 40 % and 20 % of the total contributions. (*c*) Corresponding contributions to $\langle \phi'_A \phi'_B \rangle$ divided into eight equispaced contours with warm colours denoting positive contributions and cold colours denoting negative contributions.

3.2.1. *Spatial evolution of* $P(\Phi_A, \Phi_B)$

Figure 8 shows $P(\Phi_A, \Phi_B)$ at four streamwise locations ($x = 2.5$, 5, 10, 20) and three cross-stream locations ($z = 0$, 0.5, 1) for $Re = 1500$ and $\widetilde{S} = 1.4$. We begin by considering the streamwise evolution of $P(\Phi_A, \Phi_B)$, focusing on the centreline between the jets ($z = 0$, bottom row of figure 8). Due to geometric symmetry (see figure 1), centreline occurrences of Φ_A and Φ_B are equally probable and $P(\Phi_A, \Phi_B)$ at $z = 0$ is symmetric about the line $\Phi_A = \Phi_B$.

At $x = 2.5$, filaments of Φ_A and Φ_B begin reaching the centreline while mixing with the ambient fluid, resulting in decreased concentrations of the two scalars. As a result, probabilities move in scalar space along the axes toward the origin. The most probable Φ_A or Φ_B filaments at this location fall between $0.2 \lesssim \Phi \lesssim 0.4$, as indicated by the darkest regions along the axis in figure 8. High probabilities of pure ambient
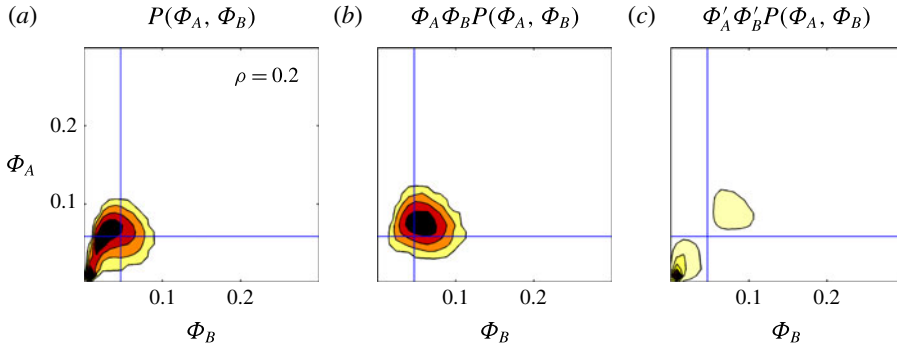
FIGURE 12. (a) The JPDF $P(\Phi_A, \Phi_B)$ for $Re = 1500$ and $\widetilde{S} = 1.4$ cm at $x = 20$, $z = 0.5$. Probabilities are shown on a log scale with contours containing 80%, 60%, 40% and 20% of the data. (b) Corresponding contributions to $\langle \Phi_A \Phi_B \rangle$ contoured to show 80%, 60%, 40% and 20% of the total contributions. (c) Corresponding contributions to $\langle \phi'_A \phi'_B \rangle$ divided into eight equispaced contours with warm colours denoting positive contributions and cold colours denoting negative contributions.

fluid result in a delta function at $(\Phi_A, \Phi_B) = (0, 0)$. Weaker probabilities of coexisting concentrations of Φ_A and Φ_B populate the interior of scalar space close to the origin, indicating that coalescence between the two only occurs after significant dilution with the ambient fluid.

By $x = 5$, many filaments of Φ_A and Φ_B have come into close proximity in attracting regions of the flow. Diffusive flux between filaments of $\Phi_A \approx 0.2$ near filaments of $\Phi_B \approx 0.2$ forms a bridge of high probability across $\Phi_A + \Phi_B \approx 0.2$. This bridge shows scalar mixing across a material interface of Φ_A and Φ_B with a minimal buffer of ambient fluid between the two. Because local mixtures of Φ_A and Φ_B are enclosed between filaments of the two scalars, $\Phi_A \Phi_B$ mixtures cannot diffuse with the ambient fluid. This results in a low-probability region located between the peak at the origin and the $\Phi_A + \Phi_B \approx 0.2$ band.

As scalar filaments continue to mix with each other, probabilities migrate away from the axes and increasingly populate the interior region of $P(\Phi_A, \Phi_B)$. At $x = 20$, Φ_A is less likely to exist apart from Φ_B and probabilities along the axis of scalar space are low.

Moving away from the centreline to the axis of the upper jet at $z = 0.5$ (middle row of figure 8), initially there will be only Φ_A diluted with ambient fluid (e.g. $x = 2.5$) and probabilities will occur along the Φ_A axis. Progressing downstream, scalar incursions of Φ_B that have mixed with Φ_A reach $z = 0.5$ and probabilities migrate off the axis. By $x = 10$ significant amounts of Φ_B are present; however, there are no structures large or energetic enough to bring pure Φ_B to the centreline of the Φ_A jet.

Outside of the two jets at $z = 1$ (top row of figure 8), ambient fluid initially dominates ($x = 2.5$). As the jets spread in the z direction, higher concentration filaments of Φ_A increase in likelihood ($x = 5$). Here Φ_B does not appear in the upper reaches of the flow until farther downstream ($x = 10$), and here only in diluted concentrations. By $x = 20$ both scalars have diluted with ambient fluid considerably and the structure of $P(\Phi_A, \Phi_B)$ has a lobed shape similar to that at $z = 0.5$, $x = 20$.

3.2.2. *Effect of jet spacing and Reynolds number on* $P(\Phi_A, \Phi_B)$

The JPDF $P(\Phi_A, \Phi_B)$ for the far jet spacing at $Re = 1500$ are shown in figure 9. Note that statistics for $z = 1$ are not shown due to the very low probabilities of Φ_B reaching this location in the study section. Along the centreline between the two jets (bottom row of figure 9), the streamwise evolution of $P(\Phi_A, \Phi_B)$ follows a similar pattern to that of the close jet spacing, although the patterns for any given value of $x = \widetilde{x}/\widetilde{S}$ are dissimilar. The on-axis nature of $P(\Phi_A, \Phi_B)$ persists farther downstream than for the close jet spacing, and because the scalars have more time to dilute with ambient fluid, overlap between the two scalars occurs at lower concentrations than at the close spacings.

Along the centreline the point at which the mean jet profiles overlap scales as $\widetilde{x}/\widetilde{S}$. Because the jets have little influence on one another the marginal PDF for each scalar, $P(\Phi)$, will evolve the same for both jet spacings at given locations of $\widetilde{x}$. Because $P(\Phi_A, \Phi_B)$ is dependent on both, there is no expectation of simple scaling of $P(\Phi_A, \Phi_B)$ with $\widetilde{x}$ or $x = \widetilde{x}/\widetilde{S}$, and it is not expected that $P(\Phi_A, \Phi_B)$ in figures 8 and 9 will be similar at given values of x.

Figure 10 shows $P(\Phi_A, \Phi_B)$ for the low Reynolds number and close jet spacing. Due to the decreased Reynolds number, filaments are much slower to converge toward attracting regions, and initially the majority of contributions to $P(\Phi_A, \Phi_B)$ lie along the axes. Mixing occurs by dilution with ambient fluid, and the bridging seen in the high-Reynolds-number case (figure 8) is no longer present.

3.2.3. *Contributions to* $P(\Phi_A, \Phi_B)$

In § 3.1 the instantaneous contributions toward the scalar overlap $\Phi_A\Phi_B$ and scalar covariance $\phi'_A\phi'_B$ are determined (figures 6 and 7). The distribution in scalar space of instantaneous contributions to $\Phi_A\Phi_B$ and $\phi'_A\phi'_B$ can be obtained by appropriately weighting $P(\Phi_A, \Phi_B)$. To illustrate, $P(\Phi_A, \Phi_B)$ at two locations, $x = 5$, $z = 0$ and $x = 20$, $z = 0.5$ (shown previously in figure 8), is shown in figures 11(*a*) and 12(*a*). At $x = 5$, $z = 0$ the majority of the probabilities fall along the axes, where one scalar occurs without the other present, or just off the axes, where one scalar with strong concentration co-occurs with a low concentration of the other. There also exists a bridge along the line $\Phi_A + \Phi_B \approx 0.2$ where diffusion is mixing scalars of neighbouring filaments. At $x = 20$, $z = 0.5$ probabilities are skewed toward Φ_A due to the transverse position of this location. Here it is unlikely to observe Φ_A apart from Φ_B, and probabilities along each axis are small.

Contributions to $\Phi_A\Phi_B$ can be found by weighting $P(\Phi_A, \Phi_B)$ by the local value $\Phi_A\Phi_B$. Note that integrating these weighted distributions across the entire scalar space yields the total mean overlap,

$$\langle \Phi_A\Phi_B \rangle = \int_0^1 \int_0^1 \Phi_A\Phi_B P(\Phi_A, \Phi_B)\mathrm{d}\Phi_A\mathrm{d}\Phi_B. \tag{3.1}$$

Figures 11(*b*) and 12(*b*) illustrate the contributions to $\langle \Phi_A\Phi_B \rangle$ for the same locations in figures 11(*a*) and 12(*a*). At $x = 5$, $z = 0$ the majority of the contributions fall in the region $\Phi_A + \Phi_B \gtrsim 0.2$. While regions occurring off the axes and away from the origin have higher potential reaction, regions of $P(\Phi_A, \Phi_B)$ close to (but not on) the axes have probabilities orders of magnitude greater than those away from the axes and therefore contribute a significant amount to the scalar overlap. At the farther downstream location ($x = 20$, $z = 0.5$), contributions to $\langle \Phi_A\Phi_B \rangle$ primarily come from the region away from the axes and the origin.

Contributions to $\phi'_A\phi'_B$ can be found by weighting $P(\Phi_A, \Phi_B)$ by the local value $\phi'_A\phi'_B$. Note that the JPDF of the scalar fluctuations $P(\phi'_A, \phi'_B)$ can be calculated by repositioning the origin of scalar space to the intersection of the local means. Formally, the scalar covariance can be defined from $P(\phi'_A, \phi'_B)$ as

$$\langle \phi'_A\phi'_B \rangle = \int_{-\langle\Phi_B\rangle}^{1-\langle\Phi_B\rangle} \int_{-\langle\Phi_A\rangle}^{1-\langle\Phi_A\rangle} \phi'_a\phi'_b P\left(\phi'_A, \phi'_B\right) \, \mathrm{d}\phi'_A \, \mathrm{d}\phi'_B. \tag{3.2}$$

Figures 11(*c*) and 12(*c*) illustrate the contributions to $\langle\phi'_A\phi'_B\rangle$ in eight equispaced contours with positive contributions appearing in red and negative contributions appearing in blue. Negative contributions to the scalar covariance exist in regions where one scalar exists below the mean concentration, while the other scalar exists above the mean concentration (upper left and lower right quadrants). Positive covariance contributions exist in regions where both scalars exist above the means (upper right quadrant), or where both scalars exist below the means (lower left quadrant). At $x = 5$, $z = 0$ the majority of the contributions to the scalar covariance are negative and come from regions where one scalar exists without the other along the axes. The majority of the positive contributions toward the scalar covariance are events where neither scalar is present (i.e. ambient fluid). At this location, the negative contributions outweigh the positive and $\rho < 0$. Farther downstream at $x = 20$, $z = 0.5$ the majority of the contributions to $\langle\phi'_A\phi'_B\rangle$ occur in the positive upper-right and lower-left quadrants where the two scalars coalesce and $\rho > 0$.

3.2.4. *Conditional diffusion*

At a given instant, the diffusive flux of a scalar filament is governed by the diffusion term $D\nabla^2\Phi$. The conditional diffusion $\boldsymbol{\gamma}$ is calculated by creating a histogram of the scalar concentrations weighted by the diffusion of each of the two scalars at the same point (Juneja & Pope 1996). The resulting vector function is normalized by the unweighted histogram $P(\Phi_A, \Phi_B)$ and has two vector components: $\gamma_A(\Phi_A, \Phi_B) = \langle D_A\nabla^2\Phi_A \mid (\Phi_A, \Phi_B)\rangle$ and $\gamma_B(\Phi_A, \Phi_B) = \langle D_B\nabla^2\Phi_B \mid (\Phi_A, \Phi_B)\rangle$ (equation (1.7)). The two vector components of $\boldsymbol{\gamma}$ define the transport of $P(\Phi_A, \Phi_B)$, and $\boldsymbol{\gamma}$ can be presented as a diffusion velocity displayed in scalar space as magnitudes and streamlines. Probabilities given by $P(\Phi_A, \Phi_B)$ will evolve along streamlines parallel to $\boldsymbol{\gamma}$ at the speed $|\boldsymbol{\gamma}|$. Figure 13 displays γ_A and γ_B for locations corresponding to those in figure 8.

At $x = 2.5$ filaments of each scalar have been diluted with ambient fluid, but little inter-scalar mixing has occurred. For very high or very low concentrations of Φ_A and Φ_B, streamlines are parallel to the axes, indicating the dilution of each scalar with ambient fluid (and ambient fluid with each scalar). At $0.1 \lesssim \Phi \lesssim 0.3$ streamlines diverge from the axes and move along a diagonal before converging near the local scalar means. This mixing path indicates local scalar filaments of concentration $0.1 \lesssim \Phi \lesssim 0.3$ are in close proximity to filaments of the opposing scalar, and diffusive flux is driving mixing between the two. This leads to the population of scalar space across the $\Phi_A + \Phi_B \approx 0.2$ line in the subsequent plot of $P(\Phi_A, \Phi_B)$ (compare with figure 8: $x = 5$, $z = 0$).

The magnitudes of the diffusion velocity vary considerably across scalar space (compare with Cai *et al.* 2011). Scalars that still exist in strong concentrations (e.g. $\Phi > 0.4$) have been stretched very thin, and gradients are sharp along their edges, resulting in a strong diffusive flux. Along the mixing path between the two scalars, diffusion velocities are slower. This highlights the two processes at play in
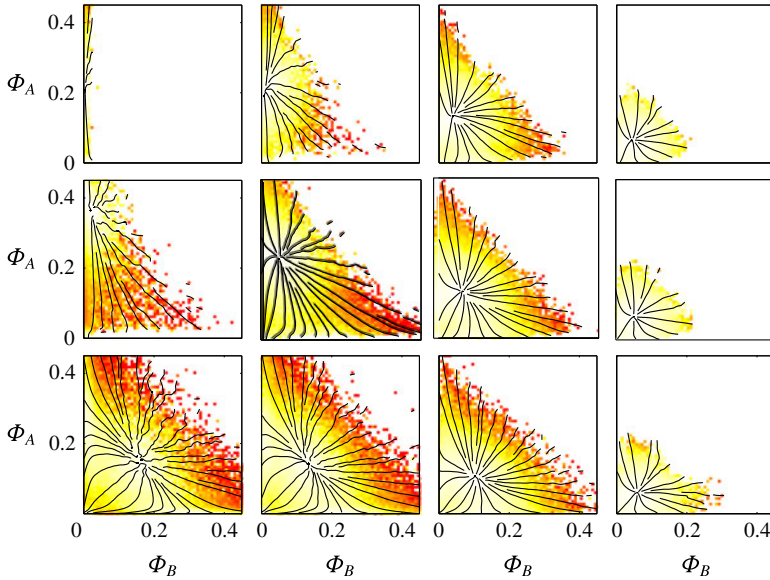
FIGURE 13. Conditional diffusion γ displayed in scalar space as a diffusion velocity for $\widetilde{S} = 1.4$ cm, $Re = 1500$ at $z = 0$, 0.5 and 1 (rows) and $x = 2.5$, 5, 10 and 20 (columns). Diffusion velocity streamlines are shown in black and magnitudes are shown ranging from white (low) to red (high).

bringing the scalars together: the fast process of turbulent stretching and folding that brings the scalars into close proximity and the slow process of diffusion that ultimately causes coalescence.

4. Summary

JPDFs are plotted for two parallel turbulent jets at multiple streamwise and transverse locations. Initially filaments of Φ_A and Φ_B exist independently of one another; however, filaments are rapidly brought close together in attracting regions of the flow (e.g. Mathur *et al.* 2007). Once the ambient buffer between filaments is small, diffusive flux brings scalars into coalescence across interfaces between the filaments. This process is accelerated as neighbouring filaments are stretched in the shared flow, sharpening gradients and increasing the diffusive flux (e.g. Crimaldi & Kawakami 2013). This is seen most prominently in the high-Reynolds-number case, where a bridge between Φ_A and Φ_B is seen in the interior region of $P(\Phi_A, \Phi_B)$. At low Reynolds numbers no bridge between filaments is seen and mixing occurs primarily through dilution with ambient fluid. The JPDFs presented in this paper highlight that the turbulent mixing between two initially distant scalars is both a nonlinear process and has non-normal distribution. The shape of the JPDFs is highly impacted by the position in the flow, as well as the initial flow conditions such as Reynolds number and jet spacing.

The JPDF $P(\Phi_A, \Phi_B)$ can be decomposed to show contributions to $\langle \Phi_A \Phi_B \rangle$ and $\langle \phi'_A \phi'_B \rangle$. Strong contributions to the mean scalar overlap occur in rare cases off the axes and away from the origin in scalar space as well as more common occurrences of coalescing scalars near the axes. Incursions from one jet into the

other initially displace the opposing scalar and result in negative contributions to the scalar covariance. Farther downstream, as diffusive flux brings filaments into coalescence, overlapping scalar filaments result in positive contributions to the scalar covariance.

The mixing path between the two scalars is of particular interest for reactive flows. The mixing path can be observed using the conditional diffusion (1.7). As probabilities evolve along the mixing path, the result is higher contributions to the mean scalar overlap and increasingly positive contributions to the scalar covariance. The diffusive path converges onto a manifold that falls along a line between neighbouring locally normal filament concentrations. Because this convergence point falls in regions where the two distant scalars have been brought together, it could be helpful in determining attracting regions in the flow.

The shape of the mixing path is complex and largely dependent on the geometry of the scalars. Similar to previous work by Cai *et al.* (2011), mixing of Φ_A and Φ_B can only occur through the ambient fluid, which results in a detour of the mixing path towards the origin in the present study. The magnitude of this detour is large in the present study likely due to the amount of ambient fluid separating the scalars, when compared with the small annulus of fluid separating scalars in Cai *et al.* (2011). The size and shape of the mixing path remain an interesting topic for future research, as it is a challenging test for mixing models.

Appendix A. Uncertainty analysis

In this appendix, individual sources of uncertainty associated with the two-channel PLIF technique are identified, and are then combined to provide an estimate of the total uncertainty in the resulting concentration measurements, Φ_A and Φ_B. This combined total can be compared with error measured in validation experiments by Soltys & Crimaldi (2011), where a range of known concentrations of mixtures of the two dyes were recorded using the two-channel system. Fluorescence response for each of the two PLIF channels was linear to within 0.5 % and cross-talk between the two channels was less than 0.3 %.

A.1. *Laser power*

The experiments used an argon-ion laser and a krypton-ion laser. Both were Coherent Innova 90C lasers operated in TEM00 mode with a closed-loop power supply. Root-mean-square (RMS) noise in the laser output is specified by the manufacturer to be no more than 0.2 %. Because the measured concentrations are directly proportional to laser intensity, this noise will linearly affect the concentration measurements for both scalars.

A.2. *pH, temperature and background dye*

Error in local concentration measurements can arise due to the sensitivity of the dyes' fluorescence to pH and temperature. Because the experiment runs over a long period of time, error in instantaneous measurements can also arise from the buildup of background dye in the flume over time. A robust post-processing algorithm, introduced in (2.1) and (2.2), can correct for these errors using measurements of the background fluorescence (Crimaldi 2008; Soltys & Crimaldi 2011). Because the dyes are introduced at a constant rate throughout the experiment and mixed into the background in the flume recirculation process, the background dye concentrations are

expected to increase linearly over time. Linear interpolation in time of background concentration images taken before and after the experiment are used as estimates for the background fluorescence at any given time during the experiment. Assuming the pH and temperature also vary gradually, and with no local fluctuations, these background images can also be used to directly correct for the change in fluorescence with pH and temperature.

As a worst-case error estimate, the maximum measurement error resulting from temperature fluctuations can be estimated using an exponential curve of the form $F = F_0 e^{nT}$ (Smart & Laidlaw 1977), where n is a constant on the order of 0.001 for the dyes used in the present study. Temperature was monitored throughout the experiments and varied no more than 1 °C, resulting in a maximum measurement error of 0.4 %. Because no reactions occur, it is reasonable to assume that pH remains constant in the neutral range over the course of the experiment.

A.3. *Photobleaching*

Photobleaching occurs when fluorescent dye molecules are exposed to high light intensities for long periods of time and are irreversibly converted to colourless leuco-compounds. While photobleaching can induce significant errors in laser-induced fluorescence measurements made with single-point techniques, it has been shown that the extent of photobleaching in planar configurations is minimal, especially in turbulent flows and when using scanning mirrors. Using a model developed by Larsen & Crimaldi (2006) we estimate the error due to photobleaching in the present system to be <0.3 %. This is a worst-case estimate in that it assumes a parcel of dye remains in the light sheet over the entire 20 cm imaging region, which is unlikely due to the turbulent nature of the flow. The model also neglects the fact that the image area is more prone to quenching, where dye molecules can recover between scans, rather than irreversible photobleaching (Song *et al.* 1997).

A.4. *Laser optics*

Laser profiles used in the experiments have a Gaussian cross-section and are focused in the test section using a series of lenses so that the beam diameter (0.5 mm) is less than one pixel (1.5 mm). Although the beam diameter is not constant through the test section, the focal length is long enough that the beam remains smaller than one pixel across the entire image region and thus can be considered constant. The laser was scanned across the image using a single mirror actuated by a galvanometer (e.g. Catrakis & Dimotakis 1996; Crimaldi & Koseff 2001) controlled by an analogue voltage signal from a signal generator. If the time resolution of the voltage signal is too coarse, bands of high and low laser intensity forming along rays emanating from the rotating mirror will be present in the unprocessed images. If the bands occur at inconsistent positions throughout the experiment there will be variability in concentration measurements. The signal generator used is capable of generating voltage with an accuracy of 0.0044 % with a time resolution of 1 MS s^{-1}. In the present configuration, this results in an uncertainty in the beam position of 3 % when compared with the width of a pixel. Considering the Gaussian nature of the beam and integrating over the width of a pixel, this results in a concentration measurement error of <0.3 %. It should be noted that the high sample rate from the signal generator in combination with the rotational inertia of the mirror both serve to smooth the laser path across the light sheet, which will considerably reduce this error in the present study.
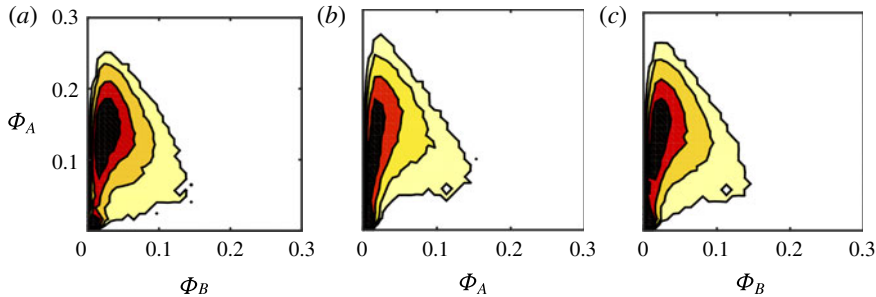
FIGURE 14. The JPDF $P(\Phi_A, \Phi_B)$ for $Re = 1500$ and $\widetilde{S} = 1.4$ cm at $x = 10$, $z\pm = 0.5$, along with the average of the two locations: (*a*) $z = 0.5$; (*b*) $z = -0.5$; (*c*) $\langle P(\Phi_A, \Phi_B) \rangle$. Probabilities are shown on a log scale with contours containing 80%, 60%, 40%, and 20% of the data.

A.5. *Attenuation*

Error in local concentration measurements can arise both from the attenuation of the laser as it passes through filaments of dye and variations in the light sheet due to imperfections in the laser optics. Laser attenuation from filament dye is avoided if the system is optically thin (i.e. uses low dye concentrations and short path lengths) (Melton & Lipp 2003). Attenuation from the background dye is directly corrected for using (2.1) and (2.2) (Crimaldi 2008).

A.6. *Cameras*

Fluorescence was imaged using a pair of Imperx Bobcat ICL-B1410 cameras. The RMS noise for these cameras is 0.1%, which is directly propagated to error in concentration measurements. The cameras both have identical lenses and are rectified to the image plane using a calibration grid. A standard 2D spatial transformation is applied to correct skew, lens distortion and translation errors (e.g. Brown 1992; Heikkila & Silvén 1997; Zhang 1999).

A.7. *Total error*

Assuming all errors are independent and random, the total error should be equal to the square root of the sum of the squares of the individual errors listed in the previous sections (Lavertu, Mydlarski & Gaskin 2008), including the cross-talk error measured in Soltys & Crimaldi (2011). This results in a total error of 0.7% for both channels, which is comparable to the experimentally measured error of 0.5% from previous studies. The calculated error is likely larger than the measured error due to the fact that many of the errors calculated above are worst-case scenarios, and not all of the errors listed above are independent and random.

As a representative illustration of the accuracy predicted by this error analysis, figure 14 shows $P(\Phi_A, \Phi_B)$ at $z = \pm 0.5$ and $x = 10$. Due to experimental symmetry, it is expected that data from a point above the centerline in scalar A should be identical to the transpose of the data below the centreline in scalar B. Visual comparison shows similar features with the majority of probabilities lying near the axis and a protrusion forming along the line $\Phi_A + \Phi_B = 0.2$. The average of the two plots shows similar features and suggests no significant consequence from averaging data from $z < 0$ with the $z > 0$ data, and is consistent with the small predicted error in the present system.

A.8. *Differential diffusion*

Some of the small differences in $P(\Phi_A, \Phi_B)$ at $z = \pm 0.5$ may be attributed to differential diffusion of the two dyes. Previous studies in low-Reynolds-number aqueous flows determined that differential diffusion can be significant at Schmidt number ratios as low as 4 (e.g. Saylor & Sreenivasan 1998; Brownell & Su 2008; ?). Effects ranged from blurring of filaments to changes in structures at scales larger than the Batchelor scale, but smaller than the Kolmogorov micro-scales. In low-Reynolds-number water jets it is estimated that the scales of anomalies caused by differential diffusion (Saylor & Sreenivasan 1998) will be smaller than the resolution of the two-channel system across the imaging region. It is expected that effects from differential diffusion are small, but may still contribute some error when calculating scalar overlap. The role of differential diffusion on co-occurring concentrations of initially distant scalars remains an interesting area for further research.

REFERENCES

ANDERSON, E. A. & SPALL, R. E. 2001 Experimental and numerical investigation of two-dimensional parallel jets. *Trans. ASME J. Fluids Engng* **123** (2), 401–406.

BALL, C. G., FELLOUAH, H. & POLLARD, A. 2012 The flow field in turbulent round free jets. *Prog. Aerosp. Sci.* **50**, 1–26.

BECKER, H. A. & BOOTH, B. D. 1975 Mixing in the interaction zone of two free jets. *Am. Inst. Chem. Engrs J.* **21** (5), 949–958.

BETA, C., SCHNEIDER, K., FARGE, M. & BOCKHORN, H. 2003 Numerical study of mixing of passive and reactive scalars in two-dimensional turbulent flows using orthogonal wavelet filtering. *Chem. Engng Sci.* **58**, 1463–1477.

BILGER, R. W., SAETRAN, L. R. & KRISHNAMOORTHY, L. V. 1991 Reaction in a scalar mixing layer. *J. Fluid Mech.* **233**, 211–242.

BROWN, L. G. 1992 A survey of image registration techniques. *ACM Comput. Surv.* **24** (4), 325–376.

BROWNELL, C. J. & SU, L. K. 2008 Planar laser imaging of differential molecular diffusion in gas-phase turbulent jets. *Phys. Fluids* **20** (3), 035109.

BUNDERSON, N. E. & SMITH, B. L. 2005 Passive mixing control of plane parallel jets. *Exp. Fluids* **39** (1), 66–74.

CAI, J., DINGER, M. J., LI, W., CARTER, C. D., RYAN, M. D. & TONG, C. 2011 Experimental study of three-scalar mixing in a turbulent coaxial jet. *J. Fluid Mech.* **685**, 495–531.

CATRAKIS, H. J. & DIMOTAKIS, P. E. 1996 Mixing in turbulent jets: scalar measures and isosurface geometry. *J. Fluid Mech.* **317**, 369–406.

CETEGEN, B. M. & SIRIGNANO, W. A. 1990 Study of mixing and reaction in the field of a vortex. *Combust. Sci. Technol.* **72** (4), 157–181.

CHAMPAGNE, F. H. & WYGNANSKI, I. J. 1971 An experimental investigation of coaxial turbulent jets. *Intl J. Heat Mass Transfer* **14** (9), 1445–1464.

COSTA-PATRY, E. & MYDLARSKI, L. 2008 Mixing of two thermal fields emitted from line sources in turbulent channel flow. *J. Fluid Mech.* **609**, 349–375.

CRIMALDI, J. P. 2008 Planar laser induced fluorescence in aqueous flows. *Exp. Fluids* **44** (6), 851–863.

CRIMALDI, J. P. 2012 The role of structured stirring and mixing on gamete dispersal and aggregation in broadcast spawning. *J. Expl Biol.* **215**, 1031–1039.

CRIMALDI, J. P. & BROWNING, H. S. 2004 A proposed mechanism for turbulent enhancement of broadcast spawning efficiency. *J. Mar. Syst.* **49**, 3–18.

CRIMALDI, J. P., CADWELL, J. R. & WEISS, J. B. 2008 Reaction enhancement of isolated scalars by vortex stirring. *Phys. Fluids* **20** (7), 073605.

CRIMALDI, J., HARTFORD, J. & WEISS, J. 2006 Reaction enhancement of point sources due to vortex stirring. *Phys. Rev.* E **74**, 1–4.

CRIMALDI, J. P. & KAWAKAMI, T. R. 2013 Reaction of initially distant scalars in a cylinder wake. *Phys. Fluids* **25**, 053604.

CRIMALDI, J. P. & KOSEFF, J. R. 2001 High-resolution measurements of the spatial and temporal scalar structure of a turbulent plume. *Exp. Fluids* **31** (1), 90–102.

CROW, S. C. & CHAMPAGNE, F. H. 1971 Orderly structure in jet turbulence. *J. Fluid Mech.* **48** (03), 547–591.

DAHM, W. J. A. & DIMOTAKIS, P. E. 1990 Mixing at large Schmidt number in the self-similar far field of turbulent jets. *J. Fluid Mech.* **217**, 299–330.

DAVIES, B. M. & JONES, C. D. 2000 Some field experiments on the interaction of plumes from two sources. *Q. J. R. Meteorol. Soc.* **126**, 1343–1366.

DUPLAT, J. & VILLERMAUX, E. 2008 Mixing by random stirring in confined mixtures. *J. Fluid Mech.* **617**, 51–86.

DURST, F., RAY, S., ÜNSAL, B. & BAYOUMI, O. A. 2005 The development lengths of laminar pipe and channel flows. *Trans. ASME J. Fluids Engng* **127** (6), 1154–1160.

ERDEM, G. & ATH, V. 2002 Interaction of two parallel rectangular jets. In *Proceedings from the 23rd Congress of International Council of the Aeronautical Sciences, 8–13 September, 2002, Toronto, Canada*. Paper ICAS 2002-R15.

ESWARAN, V. & POPE, S. B. 1988 Direct numerical simulations of the turbulent mixing of a passive scalar. *Phys. Fluids* **31** (3), 506–520.

FUJISAWA, N., NAKAMURA, K. & SRINIVAS, K. 2004 Interaction of two parallel plane jets of different velocities. *J. Vis.* **7** (2), 135–142.

GIRIMAJI, S. S. 1991 Assumed β-PDF model for turbulent mixing: validation and extension to multiple scalar mixing. *Combust. Sci. Technol.* **78**, 177–196.

GRANDMAISON, E. W. & ZETTLER, N. L. 1989 Turbulent mixing in coflowing plane jets. *Can. J. Chem. Engng* **67** (6), 889–897.

HEIKKILA, J. & SILVÉN, O. 1997 A four-step camera calibration procedure with implicit image correction. In *Proceedings of the 1997 IEEE Computer Society Conference on Computer Vision and Pattern Recognition*, pp. 1106–1112. IEEE.

HODGSON, J. E., MOAWAD, A. K. & RAJARATNAM, N. 1999 Concentration field of multiple circular turbulent jets. *J. Hydraul. Engng ASCE* **37** (2), 249–256.

HUSSEIN, H. J., CAPP, S. P. & GEORGE, W. K. 1994 Velocity measurements in a high-Reynolds-number, momentum-conserving, axisymmetric, turbulent jet. *J. Fluid Mech.* **258**, 31–75.

JAYESH & WARHAFT, Z. 1991 Probability distribution of a passive scalar in grid-generated turbulence. *Phys. Rev. Lett.* **67** (25), 3503–3506.

JUNEJA, A. & POPE, S. B. 1996 A DNS study of turbulent mixing of two passive scalars. *Phys. Fluids* **8** (8), 2161–2184.

KOMORI, S., HUNT, J. C. R., KANZAKI, T. & MURAKAMI, Y. 1991 The effects of turbulent mixing on the correlation between two species and on concentration fluctuations in non-premixed reacting flows. *J. Fluid Mech.* **228**, 629–659.

LARSEN, L. G. & CRIMALDI, J. P. 2006 The effect of photobleaching on PLIF. *Exp. Fluids* **41** (5), 803–812.

LAVERTU, T. M., MYDLARSKI, L. & GASKIN, S. J. 2008 Differential diffusion of high-Schmidt-number passive scalars in a turbulent jet. *J. Fluid Mech.* **612**, 439–475.

LIN, Y. F. & SHEU, M. J. 1990 Investigation of two plane parallel unventilated jets. *Exp. Fluids* **10**, 17–22.

MAO, K. W. & TOOR, H. L. 1971 Second-order chemical reactions with turbulent mixing. *Ind. Engng Chem. Fundam.* **10** (2), 192–197.

MATHUR, M., HALLER, G., PEACOCK, T., RUPPERT-FELSOT, J. & SWINNEY, H. 2007 Uncovering the Lagrangian skeleton of turbulence. *Phys. Rev. Lett.* **98** (14), 144502.

MELTON, L. A. & LIPP, C. W. 2003 Criteria for quantitative (PLIF) experiments using high-power lasers. *Exp. Fluids* **35** (4), 310–316.

MITARAI, S., RILEY, J. J. & KOSÁLY, G. 2005 Testing of mixing models for Monte Carlo probability density function simulations. *Phys. Fluids* **17**, 047101.

NICKELS, T. B. & PERRY, A. E. 1996 An experimental and theoretical study of the turbulent coflowing jet. *J. Fluid Mech.* **309**, 157–182.

PANI, B. & DASH, R. 1983 Three-dimensional single and multiple free jets. *J. Hydraul. Engng ASCE* **109** (2), 254–269.

POPE, S. B. 1985 PDF methods for turbulent reactive flows. *Prog. Energy Combust. Sci.* **11**, 119–192.

ROWINSKI, D. H. & POPE, S. B. 2013 An investigation of mixing in a three-stream turbulent jet. *Phys. Fluids* **25** (10), 105105.

SAWFORD, B. L. & DE BRUYN KOPS, S. M. 2008 Direct numerical simulation and Lagrangian modeling of joint scalar statistics in ternary mixing. *Phys. Fluids* **20** (9), 095106.

SAWFORD, B. L., FROST, C. C. & ALLAN, T. C. 1985 Atmospheric boundary-layer measurements of concentration statistics from isolated and multiple sources. *Boundary-Layer Meteorol.* **31**, 249–268.

SAYLOR, J. R. & SREENIVASAN, K. R. 1998 Differential diffusion in low Reynolds number water jets. *Phys. Fluids* **10** (5), 1135–1146.

SIRIVAT, A. & WARHAFT, Z. 1981 The mixing of passive helium and temperature fluctuations in grid turbulence. *J. Fluid Mech.* **120**, 475–504.

SMART, P. .L. & LAIDLAW, I. M. S. 1977 An evaluation of some fluorescent dyes for water tracing. *Water Resour. Res.* **13** (1), 15–33.

SOLTYS, M. A. & CRIMALDI, J. P. 2011 Scalar interactions between parallel jets measured using a two-channel PLIF technique. *Exp. Fluids* **50**, 1625–1632.

SONG, L., VAN GIJLSWIJK, R. P. M., YOUNG, I. T. & TANKE, H. J. 1997 Influence of fluorochrome labeling density on the photobleaching kinetics of fluorescein in microscopy. *Cytometry* **27**, 213–223.

SPALL, R. E., ANDERSON, E. A. & ALLEN, J. 2004 Momentum flux in plane, parallel jets. *Trans. ASME J. Fluids Engng* **126** (4), 665–670.

STAPOUNTZIS, H. 1988 Covariance and mixing of temperature fluctuations from line sources in grid turbulence. In *2nd International Symposium Transport Phenomena, Tokyo* (ed. M. Hirata & N. Kasagi), Hemisphere.

STAPOUNTZIS, H., WESTERWEEL, J., BESSEM, J. M., WESTENDORP, A. & NIEUWSTADT, F. T. M. 1992 Measurement of product concentration of two parallel reactive jets using digital image processing. *Appl. Sci. Res.* **49** (3), 245–259.

TONG, C. & WARHAFT, Z. 1995 Passive scalar dispersion and mixing in a turbulent jet. *J. Fluid Mech.* **292**, 1–38.

VENKATARAMANI, K. S., TUTU, N. K. & CHEVRAY, R. 1975 Probability distributions in a round heated jet. *Phys. Fluids* **18** (11), 1413–1420.

VILLAFRUELA, J. M., CASTRO, F. & PARRA, M. T. 2008 Experimental study of parallel and inclined turbulent wall jets. *Exp. Therm. Fluid Sci.* **33** (1), 132–139.

VILLERMAUX, E. 2004 Simple ideas on mixing and fragmentation. *Chaos* **14** (3), 924–932.

VILLERMAUX, E. & DUPLAT, J. 2003 Mixing as an aggregation process. *Phys. Rev. Lett.* **91** (18), 184501.

VISWANATHAN, S. & POPE, S. B. 2008 Turbulent dispersion from line sources in grid turbulence. *Phys. Fluids* **20**, 101514.

WANG, H. J. & DAVIDSON, M. J. 2003 Jet interaction in a still ambient fluid. *J. Hydraul. Engng.* **129** (5), 349–357.

WANG, C. S., LIN, Y. F. & SHEU, M. J. 1993 Measurements of turbulent inclined plane dual jets. *Exp. Fluids* **16** (1), 27–35.

WARHAFT, Z. 1984 The interference of thermal fields from line sources in grid turbulence. *J. Fluid Mech.* **144**, 363–387.

WARHAFT, Z. 2000 Passive scalars in turbulent flows. *Annu. Rev. Fluid Mech.* **32** (1), 203–240.

YUU, S., SHIMODA, F. & JOTAKI, T. 1979 Hot wire measurement in the interacting two-plane parallel jets. *Am. Inst. Chem. Engrs J.* **25** (4), 676–685.

ZARRUK, G. A. & COWEN, E. A. 2008 Simultaneous velocity and passive scalar concentration measurements in low Reynolds number neutrally buoyant turbulent round jets. *Exp. Fluids* **44** (6), 865–872.

ZHANG, Z. 1999 Flexible camera calibration by viewing a plane from unknown orientations. In *Int. Conf. Comput. Vis., Corfu, Greece*, pp. 666–673.